Journal of Molecular Catalysis A: Chemical 417 (2016) 89–100

Contents lists available at ScienceDirect

Journal of Molecular Catalysis A: Chemical

journal homepage: www.elsevier.com/locate/molcata

Different dye degradation mechanisms for ZnO and ZnO doped with N (ZnO:N)

Ivan Mouritys Pereira Silva[a], Gabriela Byzynski[b,c,*], Caue Ribeiro[c], Elson Longo[b]

[a] University of Sao Paulo, Sao Carlos, SP, Brazil
[b] Chemistry Department, Sao Paulo State University, UNESP, Araraquara, SP, Brazil
[c] Embrapa Instrumentation, Sao Carlos, SP, Brazil

ARTICLE INFO

Article history:
Received 13 January 2016
Received in revised form 22 February 2016
Accepted 23 February 2016
Available online 26 February 2016

Keywords:
ZnO:N
Photocatalytic activity
Degradation mechanism

ABSTRACT

Zinc oxide (ZnO) presents vast applicability in different areas. Diverse chemical elements are used in doping ZnO in order to modify desired properties—as proposed for enhanced visible photocatalytic activity through anion doping. Thus, the goal of this work is to develop a simple, fast and easy method for ZnO:N synthesis by a modified citrate precursor method. The as-prepared ZnO:N nanoparticles were utilized for dye photodegradation, in particular to study modifications in radical generation during photoactivation. The characterization of the nanoparticles confirms that the doping process affects neither particle morphology and crystalline structure, nor the bandgap of the samples. However, it largely affects photocatalytic activity for Rhodamine-B (Rhod-B) degradation, with an optimum N content for UV activity at 4% N and visible activity at 2% N. Under UV illumination, the photodegradation mechanism observed confirms that the ZnO:N nanoparticles presents clusters of *p* type ZnO:N embedded in *n* type ZnO particles endorsing the doping method as effective. These results enhance the essential comprehension of the photocatalytic activity of *n* type semiconductor doping processes and the modification of dye degradation mechanism related specially after doping.

© 2016 Elsevier B.V. All rights reserved.

1. Introduction

Currently, the interest in developing friendly environmental processes with great potential for wastewater treatment associated with lower cost and time has increased. With this scenario, Advanced Oxidation Processes (AOP) play an important role, especially for photocatalysis. These processes are technological alternatives for degradation of a large number of organic and recalcitrant molecules present in low concentrations [1]. The degradation of the molecules involves reaction with highly oxidant and non-selective species, like OH* radicals and, in some cases, oxygen atoms. One way to generate oxidative species is through the surface illumination of semiconductor nanoparticles by UV and visible light. This method presents an advantage for commercial application such as improved efficiency due to the high surface area of nanoparticles as well as their high interaction in aqueous solution [2].

Among other catalysts, Zinc oxide (ZnO) presents wide applicability in electrochemistry, optics and electronics, being used as gas sensors, UV resistant coatings, piezoelectric devices, resistors, surface acoustic wave devices and transparent conducting oxide electrodes [3]. ZnO is an *n* type semiconductor with high exciton binding energy (60 meV) [4] however, due to its wide band gap (3.37 eV), the semiconductor photocatalyst presents significant photocatalytic activity under visible light only after it has been doped with nonmetallic atoms. The doping process shifts the optical absorption of ZnO into the visible region, expanding the excitation wavelength of the semiconductor as such increasing applications areas and improving its photocatalytic activity [5].

Different elements as Sn [4], Al [6], Mn [7], Mg [8], Ag [9], S [10], N [11] are used in doping ZnO. Doped ZnO particles show remarkable characteristics compared to undoped ZnO, such as reduced band gap energy due to inter band formation between the conduction and valence bands. This important characteristic is derived from the N 2s orbital. There are controversies as to whether N doping generates donor or acceptor levels in ZnO band gap [12]. After N doping, the ZnO Fermi level shifts closer to the semiconductorís valence band, producing a large quantity of holes (electron acceptors). This characteristic could modify the *n* type semiconductor to a *p* type semiconductor, decreasing the electron transition energy between

* Corresponding author at: Sao Paulo State University, UNESP Electrochemistry and Ceramics Interdisciplinary Laboratory, LIEC, Chemistry Department Prof. Francisco Degni Street, 55 14800-060 Araraquara, SP Brazil.
E-mail address: gabi.byzynski@gmail.com (G. Byzynski).

http://dx.doi.org/10.1016/j.molcata.2016.02.027
1381-1169/© 2016 Elsevier B.V. All rights reserved.

the valence and conduction band in N doped ZnO (ZnO:N). As a result, photocatalytic activity under visible light becomes higher [12]. However, the lack of experimental ZnO:N results that probe themodification of the semiconductor based on *n* to *p* type confirms that there are impediments, especially in terms of reliability, reproducibility and stability of ZnO:N. This shows that the characterization and synthesis of this material require more attention.

The description of dye degradation are extensively present in literature for ZnO:N, however the use of scavengers solutions for propose a detailed mechanism for Rhod-B discoloration under UV and visible irradiation is another point that need more devotion. To carry out the investigation of mechanism determination experimentally is still an important issue as cited by Samadi et al. [13].

The objective of this work is to develop a simple, fast and easy method for the synthesis of ZnO:N by modified citrate precursor method and confirm the modification in the dye degradation mechanism of doping ZnO with N nanoparticles (ZnO:N). The results from Scanning electron microscopy and X-ray diffraction confirm that the doping process did not affect ZnO:N nanoparticle morphology and crystal structure. The band gap of the nanoparticles was obtained by diffuse reflectance spectroscopy and Tauc function. The nanoparticles were further characterized by Raman spectroscopy and Infrared spectroscopy, which confirmed the presence of ZnO crystalline lattice. The doping process largely affected photocatalytic activity under UV and visible irradiation for Rhodamine-B degradation and the degradation mechanism under UV irradiation was evaluated for pristine and doped samples. More importantly, a modification in the photocatalytic degradation mechanism of Rhod-B under UV illumination confirms that N doping of ZnO nanoparticles presents some *p* type ZnO:N clusters embedded in the *n* type ZnO semiconductor, endorsing the doping method as effective. These results enhances the essential comprehension of photocatalytic activity of the *n* type semiconductor doping processes and the modification of dye degradation mechanism.

2. Materials and methods

The samples were synthesized by the modified citrate precursor method. A ZnO resin was prepared by dissolving hexahydrated zinc nitrate ($Zn(NO_3)_2{\cdot}6H_2O$—Hexys®) in monohydrated citric acid ($C_6H_8O_7{\cdot}H_2O$—Hexys®) solution in the mole ratio of 1:1. Since citric acid is a strong complexant of Zn salts, by this strategy, it is possible to prepare zinc citrate solutions, stable enough to be modified by the addition of other salts, or by N-source molecule—as urea. 2 g of ZnO resin was then submitted to heat treatment at 150 °C for 2 h followed by 850 °C at 4 h. For the doping process, urea in different ratios was dissolved in 20 mL of ZnO resin before heat treatment. It is noteworthy that urea is also a good complexant, and can be partially polymerized to citrates, in a similar manner as the polymeric precursor method using ethylene diamine as linking agent [14,15]. In total, eight different samples were obtained being designated according to initial N content (w/w): 0.0% of N = SAM 01; 0.1% of N = SAM 02; 0.5% of N = SAM 03; 1.0% of N = SAM 04; 2.0% of N = SAM 05; 3.0% of N = SAM 06; 4.0% of N = SAM 07 and 5.0% of N = SAM 08. After urea addition, the samples were submitted to heat treatment similar to the undoped one.

The doped and undoped nanoparticles were characterized by a number of techniques. First of all, Scanning Electron Microscopy (SEM) images were obtained with JEOL Microscope—model JSM 6510 to examine particle morphology. To evaluate crystalline structure and crystallite size, X-ray dispersion (XRD) was used. The diffractograms were obtained with a Cu anode (λCu-Kα = 0154 nm) in the range of 2θ = 25–75 at 2 min^{-1}. ZnO crystallite size was calculated by Scherrer's equation, as shown below, using three X-ray diffraction peaks for each sample.

$$D = \frac{K\lambda}{\cos\theta\sqrt{B^2_{\text{measured}} - B^2_{\text{instrumental}}}} \quad (1)$$

where D is the crystallite size, K is a constant related to particle shape (assuming a spherical particle), λ is the wavelength (1.5406 Å), θ is the corresponding angle of the diffraction peak given in radians, and B_{measure} is the value in radians, at half height, of the diffraction peak and $B_{\text{instrumental}}$ is a constant associated with the equipment (in this case equals 0.003491 radians) [16].The surface area of the synthesized nanoparticles was measured by nitrogen adsorption isotherms, using the Brunauer–Emmett–Teller equation (BET) in an ASAP 2000 adsorption analyzer. The Raman spectra were collected (FT Raman Bruker RFS100/S) using the 1064 nm line of a 450 W YAG laser; 200 scans were used for each measurement at room temperature. Fourier Transformed Infrared spectra were also done (PerkinElmer FTIR spectrometer 1000 model) for all samples.

In order to determine the bandgap energy of the samples, diffuse reflectance measurements were done in a UV–vis-NIR(Cary 5G spectrophotometer). Diffuse reflectance spectra were obtained for all nanoparticles and the spectrum of the substrate was used as a baseline, which was obtained before measurements. The UV–vis spectra were performed in the diffuse reflectance mode (R) and for the samples band gap determination the *Kubelka Munk* function was used [17].

Nitrogen doping level was confirmed by X-ray photoelectron spectroscopy (XPS) (Thermo K-Alpha XPS _Thermo Scientific, Inc.) with radiation of AL K under vacuum condition <10–8 mbar and 400 μm spot size. The Survey spectra resolution was 1 eV with 5 scans and higher resolution spectra were 0.1 eV with 50 scans. The CasaXPS software was used for data treatment.

Electrochemical measurements were carried out in a conventional three-electrode system, connected to a computer-controlled potentiostat (AUTOLAB PGSTAT® 30). The three-electrode system contained a carbon paste solid electrode as the working-electrode, a Pt wire as the counter-electrode, and a Saturated Calomel Electrode (SCE) as the reference electrode. The ZnO and ZnO:N electrodes were prepared by mix of 20% (weight) of each sample with carbon particles (80%) (Sigma–Aldrich) and three drops of mineral oil. Electrochemical impedance spectroscopic were measured in a 5 μmol L^{-1} aqueous solution of potassium ferricyanide ($K_3Fe(CN)_6$)(Merck) and 0.1 mol L^{-1} of potassium chloride (KCl) at frequency range of 0.1 to 10 kHz, amplitude of 10 mV, with applied potential of 0.3 V vs SCE. The Mott-Schottky plots were obtained in the same conditions with 100 Hz of frequency and 10 mV of potential amplitude in potential range of −1.0 to 1.0 V vs SCE.

Rhodamine-B (Rhod-B) photo-degradation was analyzed under the influence of UVC and visible radiation by the discoloration of Rhod-B solution. For this experiment, 1 mg of each sample was added in beakers containing 20 mL of a Rhodamine-B aqueous solution at a concentration of 2.6 mg L^{-1}. Then the photodegradation was conducted in a reactor at 18 °C, illuminated by six UVC lamps (TUV Philips, 15 W, with maximum intensity at 254 nm) with constant magnetic stirring. Photodegradation under visible radiation was performed separately, using six fluorescent lamps as visible radiation emitters (Quality, 15 W, and maximum intensity at 440 nm). The photocatalytic oxidation of Rhod-B was monitored by taking UV–vis measurements (Shimadzu-UV-1601 PC spectrophotometer) at various light exposure times.

From the photocatalytic efficiency plots of the ZnO nanoparticles with different light sources, the order of the photodegradation reaction was calculated. The reaction should be of the pseudo

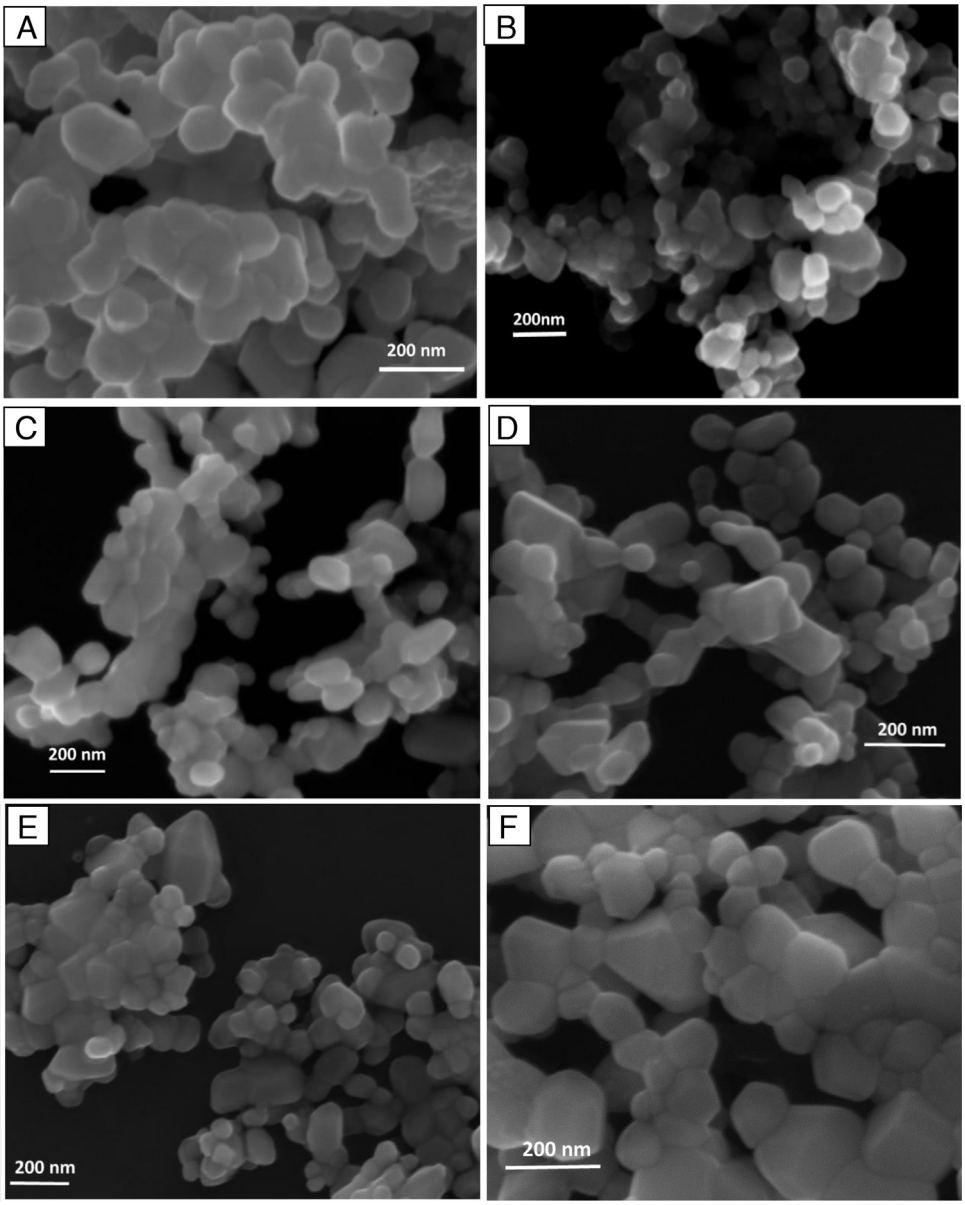

Fig. 1. Scanning electronic microscopy images (A) SAM 1, (B) SAM 4 (C) SAM 5, (D) SAM 6, (E) SAM7, (F) SAM8.

first-order with respect to Rhod-B and the kinetic law can be shown in the form of:

$$v = -\frac{d[\text{Rhod}]}{dt} = k[\text{Rhod}][\text{AS}] \quad (2)$$

where [AS] is the amount of active sites on the photocatalysts surface. As the concentration of the semiconductor is constant, the active sites amount is also constant, and could be incorporated in k. Thus, it is possible to obtain:

$$\frac{d[\text{Rhod}]}{dt} = K[\text{Rhod}] \quad (3)$$

where $K = k[\text{AS}]$ and by integrating the last equation, then:

$$-\ln\left(\frac{[\text{Rhod}]}{[\text{Rhod}]_0}\right) = Kt \quad (4)$$

In accordance with the last equation, if $[\text{Rhod}]/[\text{Rhod}]_0$ is plotted as function of t, a straight line should be obtained whose slope is K.

The photocatalytic mechanisms under UVC and visible irradiation were studied using six different scavenger substances for only four samples. The substances used were sec-butanol ($C_4H_{10}O$, 200.0 mmol L^{-1}, Merck®)(OH radicals scavenger), 2Na-EDTA ($C_{10}H_{16}N_2O_8$, 200.0 mmol L^{-1}, Synth®) (hole quencher) and P-benzoquinone (superoxide radical scavenger) ($C_6H_4O_2$, 203.0 mg L^{-1}, Merck®). The samples were SAM1, SAM5, SAM6 and SAM8. The experiments were conducted separately for each substance, adding 10 mL of the aqueous solution of each substance in different beakers followed by 1 mg of the sample and 10 mL of Rhod-B aqueous solution (5.0 mg L^{-1}), in the same manner conducted for Rhod-B photodegradation.

3. Results and discussion

3.1. Characterization of ZnO and ZnO:N nanoparticles

Fig. 1 presents SEM images of the powder samples with different N content, indicating no significant difference in particle morphology with N loading. The predominant morphology of the samples is almost heterogeneous spherical nanoparticles in the

Table 1
Crystallite size (D) and S.A. measurements (BET) for pure ZnO and N doped ZnO.

Samples	D (nm)	Surface area ($m^2\ g^{-1}$)	Band gap energy (eV)
SAM1	24	<1	3.28
SAM2	24	<1	3.28
SAM3	42	<1	3.27
SAM4	40	<1	3.28
SAM5	46	<1	3.27
SAM6	46	2.59	3.28
SAM7	50	<1	3.23
SAM8	45	3.52	3.28

form of aggregates for almost all samples. Although, as N doping increases, particle size tends to decrease and modify the surface morphology. For samples SAM 06, SAM 07 and SAM 08, hexagonal structures are easily found. However, because of the presence of aggregates formed of fine crystallites, the particle size estimated in the SEM images is not in agreement with XRD measurements. The SEM images are similar to other powders obtained by the polymeric precursor method when calcined in air, presenting aggregates with irregular surfaces for all samples [18,19].

XRD patterns for the samples present the main diffraction peaks for the wurtzite ZnO structure, which are identified in Fig. 2A. Even the doped samples present the ZnO crystalline structure, indicating that N did not interfere in crystal formation. Principal diffraction peaks corresponding to ZnO plane are presented in Fig. 2A. No characteristic peaks of impurities and other phases are observed [20,21]. After the doping process, no modification in diffraction peaks of ZnO lattice was observed, indicating that the nitrogen incorporation in the ZnO lattice or the substitution of O^{2-} by N^{3-} (substitutional N) does not modify any crystallographic parameters of ZnO lattice.

The crystallite size (D) was calculated by the Scherrer equation [16] and is presented in Table 1. It is possible to notice a positive relation between D and doping content, or an increase in crystallite size with N doping content. The superficial area (S.A.) of the samples were obtained by BET analysis, Table 1. However, due to the agglomeration or cluster formation in the samples, the S.A. values are under the technique detection.

Fig. 2B shows Raman scattering spectra for the samples but, since wurtzite nanostructures as ZnO nanostructures are symmetrized to C_{6v}, only some modes are Raman Active as E_1, E_2 and A_1. Other modes are prohibited when the incident light is perpendicular to the surface [22]. Active $E_{2(high)}$ mode at 430 cm^{-1} and $E_{2(low)}$ mode at 100 cm^{-1} are present in all samples. These Raman peaks are typical of ZnO bulk crystal and they represent the characteristic peak of wurtzite phase [22,23]. From Raman peaks at approximately 430 cm^{-1} and 100 cm^{-1}, it is possible to notice that the

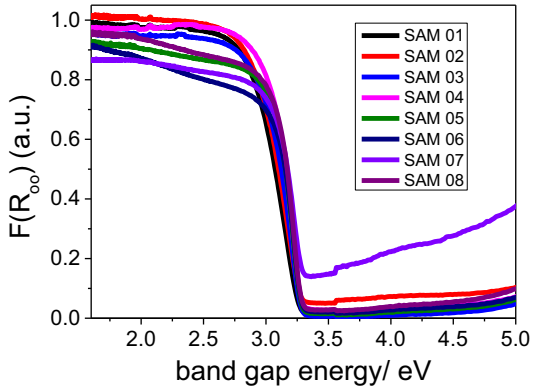

Fig. 3. *Kubelka Munk* function model. (a) SAM1, (b) SAM2, (c) SAM3, (d) SAM4, (e) SAM5, (f) SAM6, (g) SAM7, (h) SAM8.

doping process does not modify the principal crystal phase, as all the synthesized samples present this Raman active mode. Another Raman peak is identified in the spectrum samples and is similar to that present in other ZnO samples in the literature at 330 cm^{-1} [24]. Khosravi-Gandomani et al. [25] assigned the Raman peak at 330 cm^{-1} to E_{2H}–E_{2L} (multiphonon process) mode, which is an indication that ZnO is a single crystal. The E_{2H}–E_{2L} mode is present in all synthesized samples. The $E_{1(LO)}$ mode indicated at 538 cm^{-1} of the Raman spectra is associated with impurities and formation of defects such as oxygen vacancies. As the ZnO and ZnO:N samples do not present this Raman peak, it indicates higher crystalline quality and lower oxygen vacancies of the ZnO nanoparticles [25].

From the Kubelka Munk function obtained by optical diffuse reflectance spectra for the pristine and doped ZnO samples (Fig. 3), the samples present almost the same absorption behavior except for SAM 07. The maximum absorption wavelengths for the doped samples shifts to higher values with the increase in N content and thus they present visible absorption. The visible absorption is attributed to nitrogen incorporation in the crystalline lattice of ZnO [26,27]. The band gap energy presented in Table 1 was obtained by the *Kubelka Munk* function model (Fig. 3), assuming that the optical absorption coefficient corresponds to a direct transition between ZnO band structures. It can be noticed that the band gap values did not change significantly among the sample. The band gap value obtained for the pristine sample is similar to other samples synthesized with different methods (3.21 eV) [28]. However, for the doped samples, unlike TiO_2 and ZnO synthesized by other methods [28], as the N content in the doping process become higher, the band gap values do not change. On the other hand, this is not conclusive

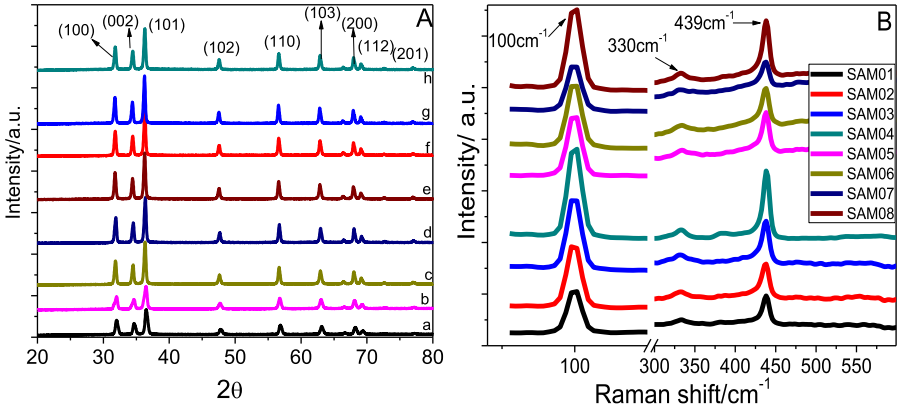

Fig. 2. (A) XRD patterns for pure ZnO and ZnO:N samples synthesized by the modified polymeric precursor method. (B)Room temperature Raman spectra of the nanoparticles. (a) SAM1, (b) SAM2, (c) SAM3, (d) SAM4, (e) SAM5, (f) SAM6, (g) SAM7, (h) SAM8.

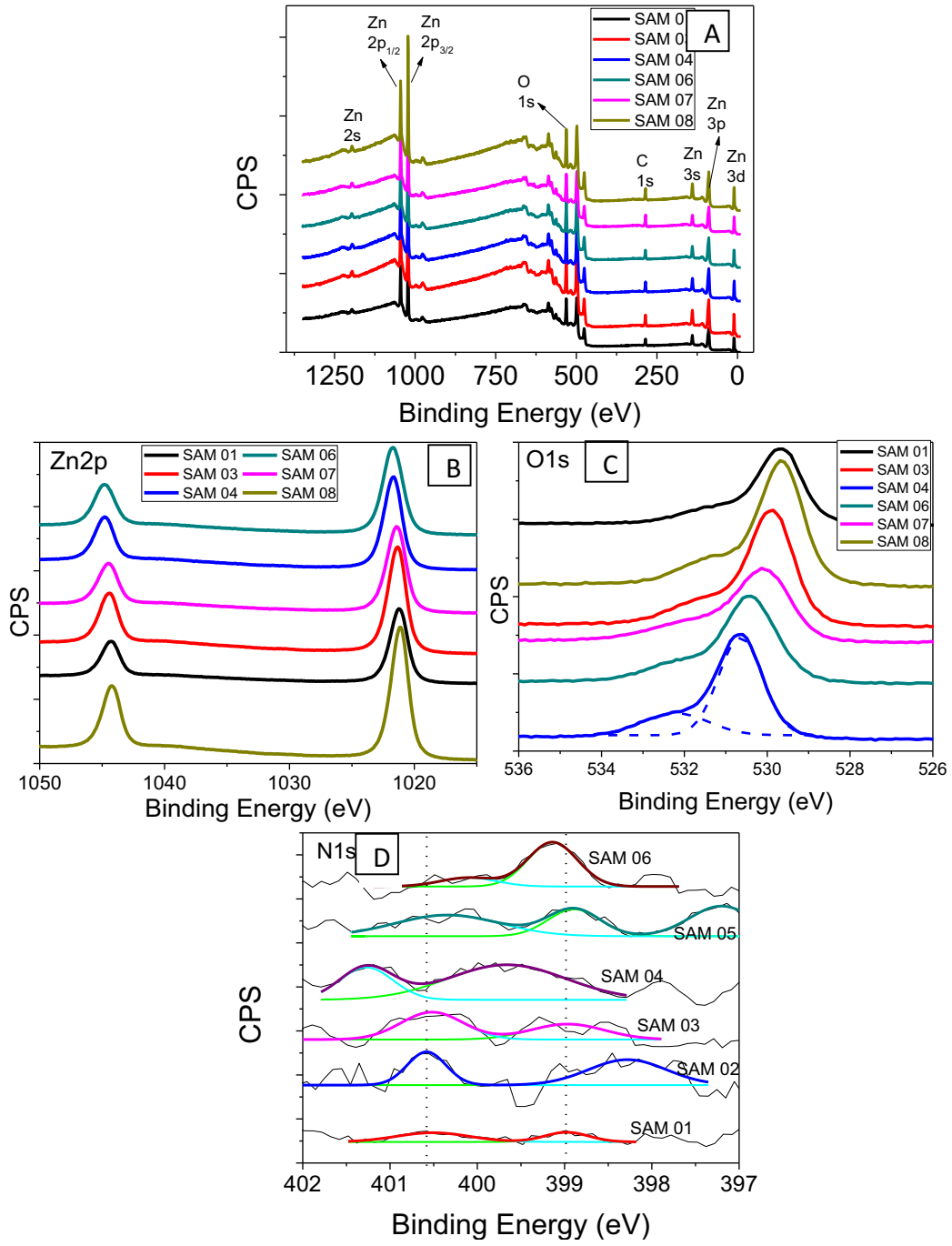

Fig. 4. (A) XPS spectra of ZnO:N and undoped (SAM 01) samples; (B) high-resolution XPS spectra of Zn 2p (C) high-resolution XPS spectra of O 1s (D) high-resolution XPS spectra of N 1s of ZnO:N and undoped (SAM 01) samples.

as intermediate levels (donor or acceptor) formed to determine a drastic change in the band gap—but sufficient to influence the other optical properties. Yu et al. [29] calculated electronic structures by density of states of ZnO nanoparticles doped with N by modified non-basic solution route, doped with NH_3 flux. Authors showed that local the intrinsic bandgap related to (0110) surface does not modify by substitutional nitrogen doping and local states of N 2p are presented as inter level energy, between valence and conduction band of ZnO. These results confirms that band-gap values modification does not change after doping process and related the visible active of doped nanoparticles through UV–vis spectra shoulders in visible region.

In order to confirm if N was incorporated into the lattice of the ZnO nanoparticle, X-ray photoelectron spectroscopy (XPS) analysis were performed for selected samples. The XPS spectra of pure and nitrogen doped ZnO nanoparticles in a wide energy range are shown in Fig. 4A for sample SAM 01, SAM 03, SAM 04, SAM 06, SAM 07 and SAM 08. The spectra are similar and the main binding energy elements (Zn, O and C) are indicated in figure, using the C 1s line as reference. Carbon is present in all samples due to easy surface contamination by carbon dioxide and some residues from the synthesis method.

For better quantification of the elements, the high resolution core level Zn 2p, O 1s and N 1s spectra were scanned and they

Table 2
Pure and N doped ZnO nanoparticles composition by XPS.

Samples	N%	C%	Zn%	O%	O(530 eV)/N
SAM 01	0.01	14.74	38.50	46.73	4255
SAM 03	0.03	18.43	35.71	45.78	1472
SAM 04	0.07	16.58	35.99	47.33	788
SAM 06	0.08	16.96	38.18	44.78	726
SAM 07	0.06	23.32	36.29	41.33	775
SAM 08	0.05	15.97	39.91	44.07	1086

are shown in Fig. 4B–D, respectively. All samples presented similar XPS spectra for each element. Zn 2 p core level spectra present two ZnO characteristic energy peaks of 1021.5–1021.9 (Zn $2p_{3/2}$) and 1044.5–1045.0 eV (Zn $2p_{1/2}$). It is possible to observe a displacement in binding energy when N content increases, indicating that the presence of N influences the Zn—O bond. The Zn $2p_{3/2}$ and $2p_{1/2}$ core lines shifts are related to the N doping process, especially the type of incorporated N [30]. O 1s core level spectra show two main peaks at 530.2–530.5 eV, corresponding to O^{2-} ions in the hexagonal wurtzite ZnO structure and 531.8–533.0 eV peaks, related to the binding energies of O—H and O_2 adsorbed on the surface of the nanoparticles [31]. The spectrum of SAM 04 presents the O 1s core lines fitted by Gaussian deconvolution to obtain both O 1s peaks (Fig. 4C). O 1s spectra also present a shift in the binding energy according to N content used in the doping process, indicating a modification in ZnO lattice after doping. However, it is noticeable that this shift is not in agreement with the initial N content (N content introduced in synthesis methods), which may indicate that for lower doping levels, N may be in the interstitial state, displacing O positions. In larger amounts, N may induce O vacancies, which means that O 1s spectra reflect the Zn-O binding energy, as seen in undoped sample.

Besides Zn and O elements, nitrogen can be seen in all samples and presents a similar spectrum for all doped samples. Although in the undoped sample (Fig. 4D) a N signal (399.87 eV) was found, related to molecular nitrogen terminally bonded and adsorbed on the nanoparticleís surface, N 1s spectra of doped sample present a dissimilar behavior as the undoped sample. Two signals are shown, the lower energy binding peak related to molecular nitrogen (399.06–400.13 eV) as for SAM 01, and the highest energy binding peak (397.57–398.70 eV) associated with N^{3-} in metallic nitrites (N—Zn bindings) [32].

The sample composition and relationship between O 1s (530 eV) and the N 1s related area are presented in Table 2. As this relation decreases, confirming the efficiency in the N doping process, two possibilities may occur: either O 1s peak area decreases or the N 1s peak area increases. It is possible to notice that O 1s percentage in the samples slightly decreased as the N content increased until an optimum value (SAM 06). This suggests N replacement of O positions (substitutional doping, ZnO:N) in the ZnO structure, resulting in the formation of energetic levels below the valence band (0.4–1.3 eV). Other elements that present this feature may be cited, as Cu, Li, Na [27]. N acts as an electron acceptor and when its concentration exceeds donor electrons sites, ZnO:N presents *p* type conduction [33]. However, the initial N content used in the method does not imply in ZnO:N *p* type conduction in the entire semiconductor, but on *p* type regions or cluster formation in the structure of the semiconductor. It should also be highlighted that there is the possibility of interstitial N doping in the ZnO crystalline structure, not allowing the *p* type semiconductor behavior [33]. Both interstitial and substitutional N doping influence photocatalytic activity in different ways, however, XPS spectra was not able to identify interstitial N. In this case, for this material, the authors consider only substitutional N doping.

The physical characteristics and the influence of N doping on electron transport properties of ZnO:N nanoparticles were investigated in more details by electrochemical impedance spectroscopy (EIS)(Fig. 5A–B) following an equivalent circuit model (inset in Fig. 5B). Solid electrodes with each ZnO:N and ZnO nanoparticles were built with carbon paste electrode. EIS results as Nyquist plots are presented in Fig. 5A–B for all synthesized samples, where imaginary numbers of impedance are plotted against the real numbers, exhibiting a semicircle for each sample, except for the carbon paste electrode. In the equivalent circuit, R_{ct}, R_s and CPE values represent charge transfer resistance, electrolyte resistance and interfacial capacitance (as seen in Table 3). For the carbon paste electrode, R_{ct} is slightly small, exhibiting a faster charge transfer compared to the others electrodes and EIS for carbon paste electrode is in the form of a straight line. A constant phase element (CPE) was used instead of a real capacitor (C) in order to consider the surface roughness of the electrodes [34,35]. From Fig. 5 and Table 3, it is possible to confirm that N doping process clearly influences R_{ct}, showing a tendency in the decrease of charge transfer resistance value as N content increases (N found in XPS analysis). The behavior indicates that the doping process decreases the electron transfer resistance and, consequently, intensify the charge mobility in ZnO:N, confirming existence of trap levels after N doping. The R_s also suffer a negative modification as N content increases, the CPE value, as expected, presents an inverse tendency of R_{ct}, i.e., CPE value increase as N content values. However, the intensification in charge mobility does not imply a rise in charge recombination. Lee et al. [34] obtained similar results with TiO_2 decorated ZnO dye sensitizing solar cell and correlated them with electron life-time, which increased when internal resistance decreased. R_{ct} values also modifies with the crystallite size (*D*) of the samples. The charge transfer resistance (R_{ct}) decreases as crystallite sizes (*D*) decreases, probably by surface area and grain boundaries effects. Mhamdi et al. [35] observed a similar behavior.

Table 3
Fitting results of ZnO solid electrodes by impedance plots based on the equivalent circuit model.

Electrodes	R_s (Ω)	R_{ct} (Ω)	CPE (μF)
Carbon paste	63.40	58.82	6.09
SAM 01	81.06	623.54	0.68
SAM 02	63.62	460.93	1.48
SAM 03	74.19	244.77	2.31
SAM 04	47.39	247.98	2.13
SAM 05	67.27	295.23	1.46
SAM 06	40.52	248.73	4.27
SAM 07	54.35	235.79	1.96
SAM 08	41.02	181.19	2.79

3.2. Photocatalytic profiles

The Oxidation/descoloration profile of Rhod-B under UVC irradiation (Fig. 6A) and under visible irradiation (Fig. 6B) show that the samples present different photocatalytic activities. Rhod-B discoloration rate is presented in Fig. 7A for UVC irradiation and Fig. 7B for visible irradiation. It is important to notice that the discoloration of Rhod-B solution does not mean that Rhod-B molecules degrade in this condition. For the confirmation about the Rhod-B degradation, it is necessary other analytical techniques, as chromatographic techniques and are not under the this work scopes. The UV illumination was conducted by six UVC lamps (TUV Philips, 15 W, with maximum intensity at 254 nm) and the visible illumination by six visible fluorescent lamps (Quality, 15 W, and maximum intensity at 440 nm). Under UVC irradiation, in Fig. 6A, it is possible to observe that N doping had a weak influence on photocatalytical activity, indicating a different result than previously presented in the literature, where ZnO doped samples showed a reduction in

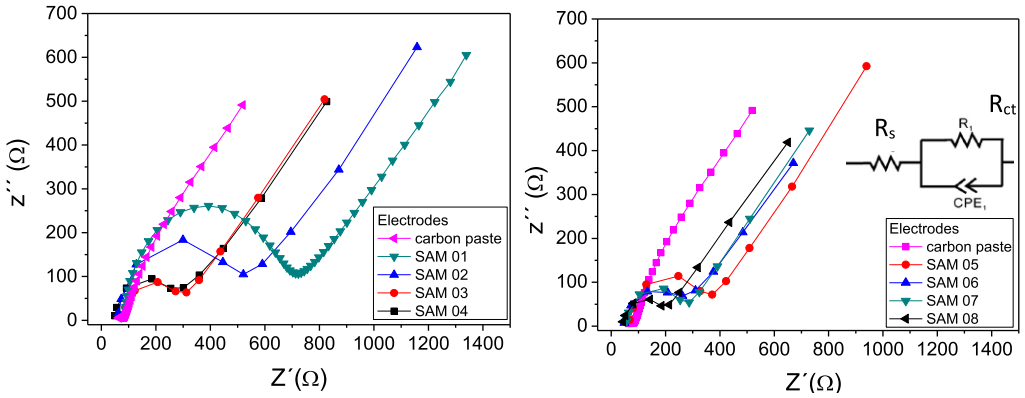

Fig. 5. Nyquist plots of the carbon paste and ZnO:N electrodes with carbon paste under 0.3 V, in 0.05 mol L^{-1} $K_3Fe(CN)_6$ and 0.1 mol L^{-1} KCl solution. Frequency range 0.1–10 kHz and amplitude 10 mV.

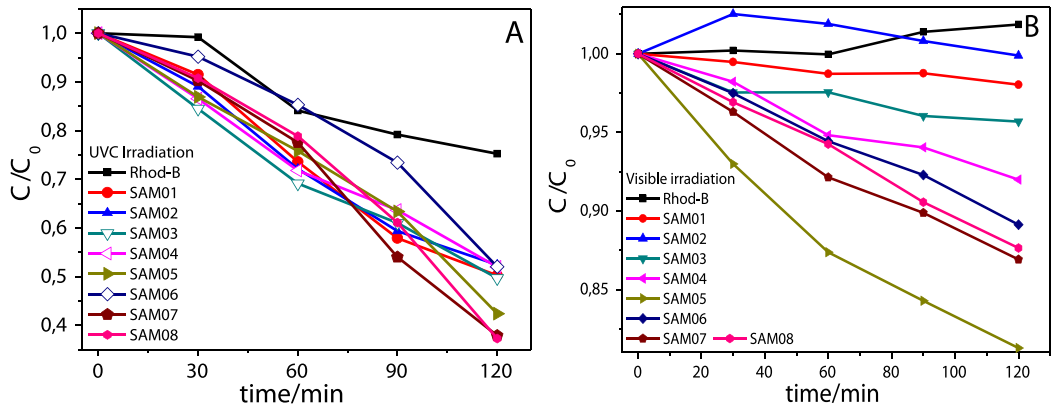

Fig. 6. Photodegradation profile of Rhod under (A) UVC radiation and (B) visible radiation.

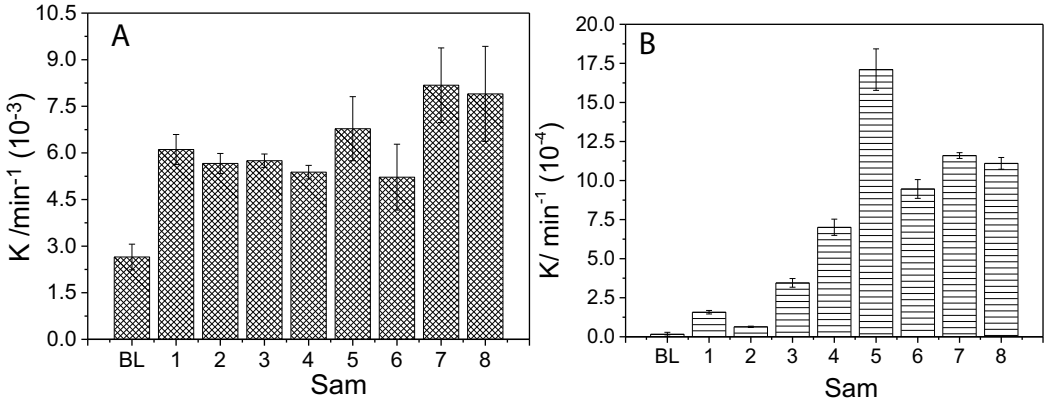

Fig. 7. Kinetic constants (k) of Rhod-B degradation for the synthesized samples (A) under UVC illumination and (B) under visible illumination.

catalytic activity [18,19,30,36,37]. However, the doping process showed an important result in photocatalytic activity in the visible range, even though the nanoparticle band gap was not modified. The increase in photocatalytic activity is not linear with N content, so it is possible to notice an optimum percentage for N doping, as presented in Fig. 7A. Rajbongshi et al. [38] attribute the elevated visible absorption of ZnO:N to high oxygen vacancies and small particles size of ZnO sol–gel synthesis and nitrogenizing by nitrogen gas flux.

In a similar manner as nitrogen doped TiO_2, nitrogen doping of ZnO is allowed to occur as substitutional or interstitial N in the ZnO lattice. In the first case, the N^{3-} atom replaces the O^{2-} in order to maintain charge neutrality, O vacancies (V_o) are generated. In the second case, interstitial doping process, N^{3-} atom is located in ZnO lattice instead of directly replacing O^{2-}. The V_o created is lower than in the first case, but it is sufficient to maintain charge neutrality. The two types of doping processes result in a contradictory effect in the nanoparticle photocatalytic activity. For TiO_2, substitutional N narrows the band gap due to the merging of N 2p states and O 2p states in the valence band. Interstitial N, on the other hand, introduces deep energy levels above the valence band gap, which may not contribute significantly to band gap narrowing and enhanced photocatalytic activity [20]. For ZnO nanoparticles, similar results may occur for different doping processes and, as presented

previously for TiO_2 [20], availability for N doping could influence in the different types of processes, resulting in different photocatalytic activity. So it is possible to conclude that an optimum N content exists. For higher N content, the degradation mechanism under UVC illumination may be modified by the inter band in the band gap energy of ZnO or defects caused by the N^{3-} atoms present in the ZnO lattice during the heat treatment. Similar results were shown by N doped Ag:ZnO nanoparticles obtained by the plasma nitriting method, presenting better photocatalytic activity due to the inter band in ZnO band gap created by the N doping process near the ZnO valence band. On the other hand, silver doping allows rapid transfer of excited electrons [20].

The new energy band created by N doping, inter band in the ZnO band gap, is related more specifically to the degradation mechanism that occurred during visible illumination. Under visible radiation (Fig. 6B and B), SAM 07 and SAM 08 showed good photocatalytic activity, but SAM 05 exhibited the highest oxidation rate for Rhod-B, also indicating an optimum N content for visible photocatalytic activity. It should be highlighted that in the visible degradation mechanism, the dye-sensitized mechanism also takes place and influences the *k* value, exhibiting elevated values. Similar to previous results, there is an optimum N content for better photocatalytic activity under visible illumination, which is around the N content of SAM 05. Similar results were obtained by ZnO:N synthesized by the one-step low temperature solvothermal process with HNO_3 as N source and by ZnO with mesoporous silica doped with N using $Zn(NO_3)_2$ as precursor [37].

Under UV light illumination, SAM 07 and SAM 08 are the samples most indicated for the photocatalytic discoloration of colored substrates, due to the *k* values presented. Under visible light illumination, the k values show the better performance for SAM 05 for the photocatalytic discoloration of colored substrates, presuming an effective enhanced photocatalysis compared to the undoped sample. However, the discoloration mechanisms needs to be better understood in each case.

3.3. Discoloration mechanisms of ZnO and ZnO:N nanoparticles

The contribution of OH^*, O_2H^* and $h^\bullet$ in the reaction mechanism under UVC irradiation was evaluated with scavenger solutions: butanol, 2Na-EDTA and *P*-benzoquinone solutions. These experiments were conducted in the same experimental condition without scavenger solution and were done separately for each solution. Only four synthetized samples were chosen for the experiment: SAM 01, SAM 05, SAM 06 and SAM 08, due to dopant content and photoactivity, since SAM 01 is the pristine sample, SAM 08 is one of the samples that presents elevated photoactivity and elevated N content, SAM 05 has medium photoactivity and SAM 06 has the lowest photoactivity under UV light illumination. The concentrations of the selected scavengers were high enough to inhibit majority of the reactive species.

Butanol solutions is considered OH^* radical scavengers, 2Na-EDTA solution is hole quenchers and P-benzoquinone acts as a superoxide radical scavenger. It is important to mention that each of these substances acts as an inhibitor for specific mechanism steps, so the photooxidation mechanisms of Rhod-B were analyzed by observing scavenger effects on the rate constants (*K*) after degradation. The UV–vis photodegradation spectra of Rhod-B were acquired and the rate constants were determined as those previously calculated. Fig. 8 shows the rate constants obtained for the samples under UV irradiation.

Fig. 8 presents the degradation efficiencies of Rhod-B (*k*) for undoped sample (SAM 01), SAM 05, SAM 06 and SAM 08 under UV illumination. The numbers shown under each scavenger column indicate the reduction in *k*, related to UV photocatalytic activity constant. The variations among the scavengers reveal that the doping process had more influence on the direct hole oxidation mechanism—as mainly revealed by SAM 08, which had the best photocatalytical activity under UV radiation. This may be related to the presence of donor levels in the bandgap, which facilitates electron suppression from the dye during photoactivation. This is an important result since it sheds light on the different ways that the doping may alter the photocatalytic profile, despite more efforts possibly being necessary to evidence all the influential variables. The degradation of dyes such as Rhodamine B may occur by two routes: (1) direct oxidation by charge transfer between dye and formed holes ($h^\bullet$) or photoelectron (eí) in the material or (2) by the generation of reactive oxygen species such as OH radicals (OH^*) and superoxide (O_2H^*). The oxidation mediated by photogenerated carriers in a photocatalyst upon incidence of radiation can oxidize the dye through its adsorption on the material, and then the electron transfer occurs between the species involved (direct oxidation), or oxidation conducted by photogenerated carriers. For the other path, OH^* radical formation occurs by the oxidation of hydroxyl ions or water adsorbed on the surface of the photocatalyst, which acts as the most common degradation mechanisms for dyes or other organic substances (indirect oxidation).

ZnO is can be considered as a noncentrosymmetric oxide due to the presence of a $[ZnO_4]$ with 4-folder tetrahedron as its basic constituent unit [39]. Then, its photocatalytic mechanism can be based on a cluster model, where magnitude and structural order-disorder effects determine the physical-chemical properties of material. The model is demonstrated below. Firstly, $[ZnO_4]^x$ may be associated with neutral (V_o^x) or mono-ionized ($V_o^\bullet$) or di-ionized ($V_o^{\bullet\bullet}$) oxygen vacancies. The hole trapping center is identified as oxygen vacancies in a disordered structure of complex clusters ($[ZnO_4]^x/[ZnO_3{\cdot}V_o^x]$).

$$[ZnO_4]^x + [ZnO_3{\cdot}V_o^x] \rightarrow [ZnO_4]' + [ZnO_3{\cdot}V_o^\bullet] \quad (5)$$

Water molecules could be adsorbed in the material surface, promoting hydroxyl radical (OH^*) production, which with O_2H^*, are principally responsible for organic substances degradation.

$$[ZnO_3{\cdot}V_o^\bullet] + H_2O \rightarrow [ZnO_3{\cdot}V_o^\bullet]...OH_{2(ads)} \quad (6)$$

$$[ZnO_3{\cdot}V_o^\bullet]...OH_{2(ads)} \rightarrow [ZnO_3{\cdot}V_o^x]...OH^*_{(ads)} + H^\bullet \quad (7)$$

Molecular oxygen could be associated with $[ZnO_3{\cdot}V_o^\bullet]$ and adsorbs on the materialís surface, promoting the link between di-ionized oxygen vacancy and cluster. The radical (OH^*) production is cited in literature as the major responsible for humic acid photodegradation by ZnO:N/ZnO heterostructures [40]. Finally, a superoxide radical (O_2H^*) will be produced to cause organic substance degradation.

$$[ZnO_3{\cdot}V_o^\bullet] + O_2 \rightarrow [ZnO_3{\cdot}V_o^\bullet]...O_{2(ads)} \quad (8)$$

$$[ZnO_3{\cdot}V_o^\bullet]...O_{2(ads)} \rightarrow [ZnO_3{\cdot}V_o^{\bullet\bullet}]...O_2'_{(ads)} \quad (9)$$

$$[ZnO_3{\cdot}V_o^{\bullet\bullet}]...O_2'_{(ads)} + H^\bullet \rightarrow [ZnO_3{\cdot}V_o^{\bullet\bullet}]...O_2H^*_{(ads)} \quad (10)$$

The results shown in Fig. 8 confirms the essential participation of OH^* radical in the oxidation of Rhod-B for undoped sample (SAM 01). Similarly, the addition of p-benzoquinone (O_2H^* quencher) results in a strong inhibition of Rhod-B photocatalytic degradation as described in the literature [41]. Even with scarce O_2H^* in solution, degradation could occur via $h^\bullet$ and OH^*. For Na-EDTA solution, slightly lower inhibition of photocatalytic activity was also obtained. This behavior suggests that holes are important in Rhod-B oxidation and the major degradation mechanism is by OH^* or O_2H^* in undoped ZnO,

For doped samples, a difference was observed in the mechanisms between SAM 06 and others (SAM 05 and SAM 08). For SAM 06, similarly as SAM 01, the hole scavengers present an inhibition in photocatalytic activity and the importance in the mechanism is

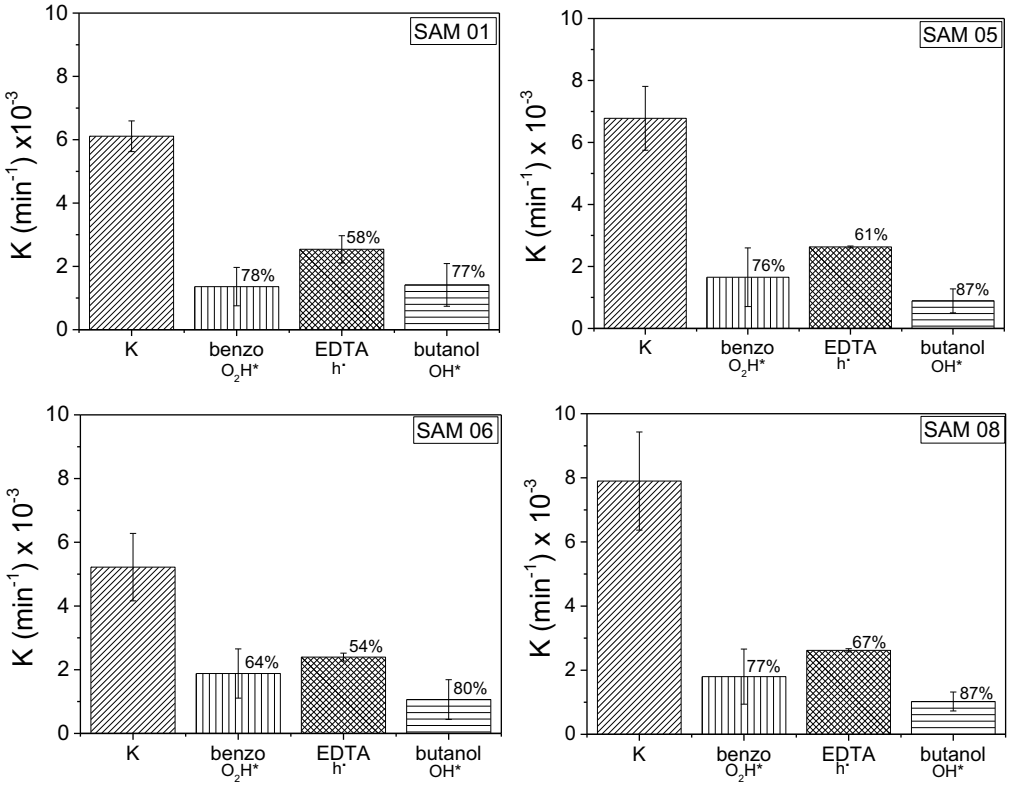

Fig. 8. *k* of Rhod-B degradation with different scavenger solutions under UV illumination.

confirmed. Although, OH* radicals present a slightly importance in the mechanism. However, contrary to the undoped sample, the superoxide radicals in the SAM 06 mechanism do not play an important role, as its inhibition is lower than the other samples. This result possibly indicates the decrease in the photocatalytic activity for this sample compared to other doped samples, as it is the less efficient sample for Rhod-B discoloration under UVC irradiation.

The samples SAM 05 and SAM 08 present OH* radicals as the principal factor for Rhod-B discoloration, even though O_2H^* is not needless. Even SAM 06 presented a slight difference, the direct oxidation of Rhod-B by holes is play an important role in degradation mechanism for doped samples as the hydroxyl radicals, indicating a modification in the Rhod-B discoloration mechanism, indicating an increase in photocatalytic activity under UVC irradiation. Thus, the photocatalytic mechanism based on a cluster model for doped samples (ZnO:N) is proposed with $[ZnO_4]^x$ associated to a neutral oxygen vacancy $[ZnO_3{\cdot}V_o{}^x]$ in the presence of an N source (N_{source}) resulting in some *p* type semiconductor clusters $[ZnO_3N]'$ inside $[ZnO_4]$.

$$[ZnO_4]^x + [ZnO_3{\cdot}V_o{}^x] + N_{source} \rightarrow [ZnO_3N]' + [ZnO_3{\cdot}V_o{}^{\bullet}] \quad (11)$$

The resulting *p* type cluster $[ZnO_3N]$í interferes in the OH* and O_2H^* radical mechanism production. For the OH* radical mechanism production, with an increase in $[ZnO_3{\cdot}V_o{}^{\bullet}]$ production in Eq. (11), the OH* radical production also increases compared to the undoped sample mechanism. The *p* type cluster $[ZnO_3N]$í reacts with H• resulting from Eq. (7) and the $[ZnO_3N]^*$ radical is produced as H_2.

$$[ZnO_3{\cdot}V_o{}^{\bullet}]\ldots OH_{2(ads)} \rightarrow [ZnO_3{\cdot}V_o{}^{x}]\ldots OH^*_{(ads)} + H^{\bullet} \quad (7)$$

$$[ZnO_3N]' + H^{\bullet} \rightarrow [ZnO_3N]^* + H_2 \quad (12)$$

In the O_2H^* radical production mechanism, a *p* type cluster $[ZnO_3N]$í inhibits the di-ionized ($V_o{}^{\bullet\bullet}$) oxygen vacancy and consequently reduces the O_2H^* radical production as presented in Eqs. (9) and (10). Therefore, the principal mode for the photocatalytic degradation mechanism is OH* radicals.

Fig. 9 presents the degradation efficiencies of Rhod-B (*k*) for undoped samples (SAM 01), SAM 05, SAM 06 and SAM 08 under visible illumination. The same scavenger solutions in UV irradiation were used for visible irradiation and the numbers shown under each scavenger column indicate the reduction in *k*, related to the visible photocatalytic activity constant. One can notice that in the case of SAM 01 and SAM06, the use of scavenger solutions increase photocatalytic activity under visible illumination. This conduct is attributed to scavenger effect on Rhod-B radicals generation. In photolysis process, without a semiconductor, the photonic degradation mechanism occurs, which is related to wavelength illumination and Rhod-B concentration, producing Rhod-B radicals that will then degraded. With such scavengers solutions, in the case of SAM 01 and SAM 06 photocatalysis, it could induce the increase in Rhod-B radicals generation, promoting an untrue increase in production of O_2H^* and h•. In this case, the remission of the scavengers constant compared with the photocatalytic constant was considered as null and the reduction in efficiency were considered as 0%.

In accordance with Fig. 9A, this result confirms the essential participation of OH* radical in the oxidation of Rhod-B even for visible illumination, indicating the main process that occurs in the photocatalytic degradation mechanism under visible illumination of SAM 01, which is different under UV illumination. For UV illumination, the main radicals responsible for Rhod-B degradation were O_2H^* and OH*.

For doped samples, similar results as UV illumination were observed. For the mechanism of SAM 06, the similarity with SAM 01 is notice and for SAM 05 and SAM 08 is evident the mechanism analogist between them. However, SAM 06 mechanism is different from SAM 05 and SAM 08. Sample SAM 06 presents, likely for UV illumination, the significance of OH* radicals in the mechanism is

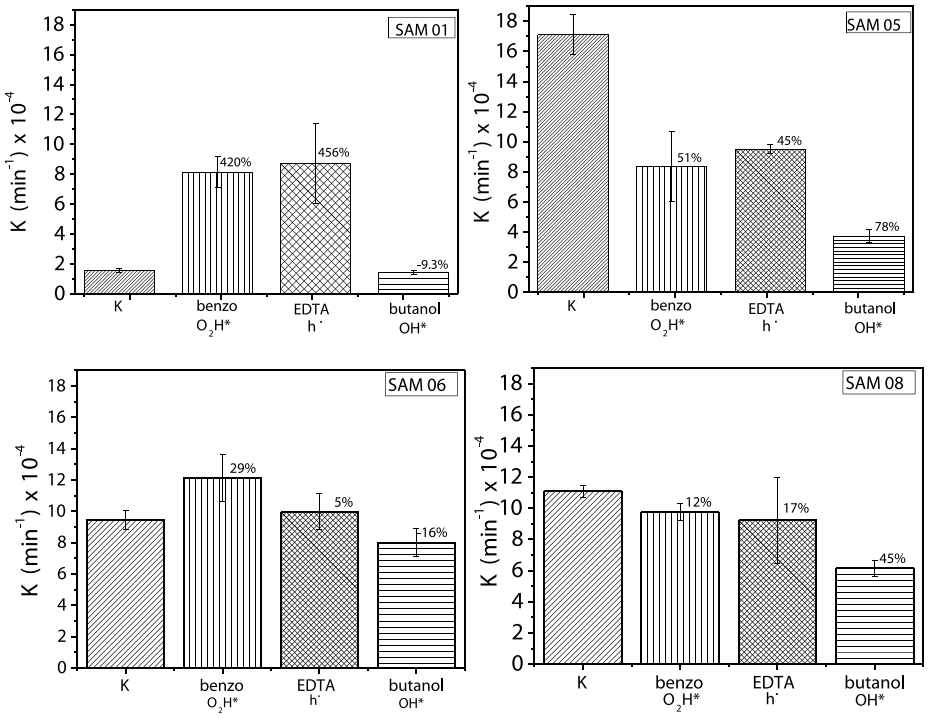

Fig. 9. *k* of Rhod-B degradation with different scavenger solutions under visible illumination.

established, and O_2H^* and h$^{\bullet}$ are not significantly important. Even though, similar results as for SAM 01 is highlighted, confirming that the degradation mechanism of SAM 06 resembles that of SAM 01 compared to SAM 05 and SAM 08.

For sample SAM 05, the OH* radicals are the principal factor for Rhod-B discoloration as presented for the undoped and SAM 06. However, the difference is that O_2H^* and h$^{\bullet}$ also participated in the degradation mechanism under visible illumination instead of only OH* in the case of SAM 01 and SAM 06. The same performance is observed for SAM 08.

Like for UV illumination, the hydroxyl radicals are significantly important in the degradation mechanism under visible irradiation. For undoped sample (SAM 01) in UV irradiation, O_2H^* and OH* were mainly the radicals involved in the Rhod-B degradation. For doped samples, under UV irradiation, only OH* was considered the main radical. In visible illumination, the doped and undoped samples presented similar mechanism, where the principal radical for Rhod-B degradation was OH*. The influence of *p* type cluster $[ZnO_3N]'$ presented in Eq. (11) is confirmed also for visible irradiation, as OH* is the main radical in the Rhod-B degradation and the *p* type cluster $[ZnO_3N]'$ inhibits the O_2H^* radical production as presented in Eqs. (9) and (10).

3.4. Mott Schottky plots and energy diagram

The difference between the photocatalytic mechanism of ZnO and ZnO:N was better investigated by electrochemistry measurements as surface charge capacitances through Mott-Schottky plots (Fig. 11), which is defined by Eq. (13):

$$\frac{1}{C_{SC}^2} = \frac{2}{q\varepsilon\varepsilon_0 N_D}\left(E - E_{FB} - \frac{kT}{q}\right) \quad (13)$$

where C_{sc} is the space charge capacitance (F cm^{-2}), q is the elementary charge, ε is the relative dieletric constant of the semiconductor, ε_0 is the permittivity of the vacuum, E is the applied potential, k is Boltzmann's constant and T is the absolute temperature. The slope and y-intercept, extrapolating a straight line, in C^{-2} against E graphics (C^{-2} vs E, Fig. 10) provide the donor density (N_D) and the flat band potential (E_{FB}) of the electrodes, respectively [42–44]. These values are shown in Table 4.

Table 4
Flat band potentials values (E_{FB}) and donor density (N_D) of synthetized samples.

Electrodes	E_{FB} vs NHE	$N_D \times 10^{10}$
SAM 01	−0.97	111.12
SAM 02	−1.11	112.23
SAM 03	−1.08	155.50
SAM 04	−1.23	3.57
SAM 05	−1.46	3.74
SAM 06	−1.21	4.76
SAM 07	−1.24	4.38
SAM 08	−1.36	1.18

As can be seen from the Mott-Schottky plots in Fig. 10A and B, all samples exhibit positive slopes when a negative potential is applied, characterizing an *n* type conductivity, in accordance with the literature [42–44]. However, for SAM 04, SAM 05, SAM 06 and SAM 07 a negative slope is observed when positive potential is applied, Fig. 10C. The positive slope is a characteristic of *p* type conductivity [42–44], confirming the existence of *p* type cluster inside the *n* type semiconductor. Although, the main *n* type conductivity is imposed trough the *p* type. Synthesis of ZnO doped with urea by microwave assisted hydrothermal method, using zinc nitrate variation to produce different particles shape were presented by Herring et al. [45]. In this article, the modification of ZnO particles *n* type properties are modified to p-type properties after N doping with large amount of urea. The confirmation of modification properties is done by Mott-Schottky analysis.

SAM 05, SAM 06, SAM 07 and SAM 08 present different intensity in Mott-Schottky plots compared with SAM 01, as shown in the inset in Fig. 10B. After the doping process, the highly doped samples (SAM 04 to SAM 08) present significantly smaller N_D values compared to undoped sample (SAM 01), because the doping process probably enhances impurity states in these materials, creating charge donor levels. In addition, SAM 02 and SAM 03

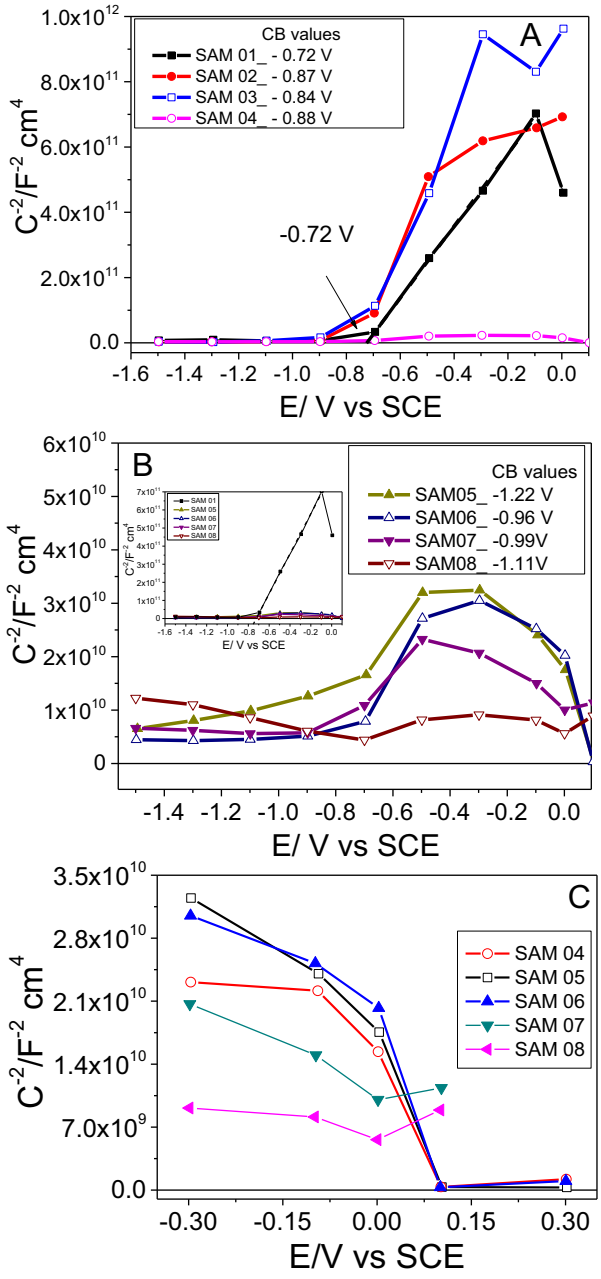

Fig. 10. Mott-Schottky plots of ZnO:N samples at fixed frequency of 159 Hz in the dark and a potential amplitude of 10 mV in NaOH (1 mol L^{-1}) solution. CB values = conduction band values obtain from Mott-Schottky plots vs SCE.

show more elevated N_D value than SAM 01, indicating an increase in the charge concentration at the space charge depletion layer. Both results confirm a distinct behavior of doped samples. In lower N content, N species works as passivation layer that reduces the surface trap states and, in more elevated N content, N species operates as donor levels, enhancing the donor density values. Moreover, it is interesting to note that E_{FB} of the N doped samples is shifted to a more negative potential compared to SAM 01, which can enrich the charge carrier separation efficiency by increasing the degree of band bending [42–44]. The main basis for the flat band potential shifts is the N-induced states that induce Fermi-level pinning.Through the flat band potential and band gap values, the conduction and valence band of each sample could be estimated. Fig. 11 illustrates the band positions of the ZnO:N electrodes, which demonstrate that the conduction band for SAM 05 is the most

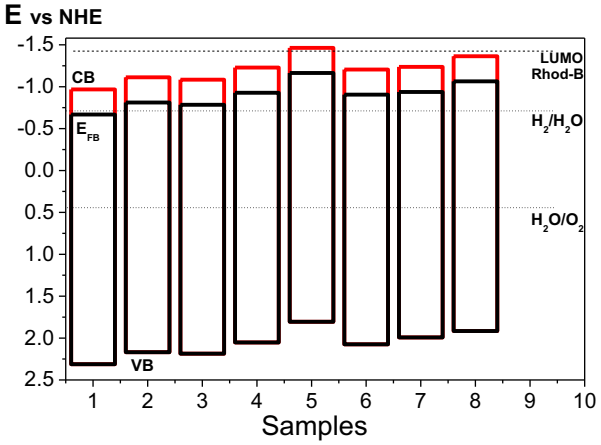

Fig. 11. Band positions of samples in carbon paste electrode in NaOH (1 mol L^{-1}) solution. CB: conduction band, VB: valence band, EFB: flat band potential.

shifted compared to others samples. In fact, it is higher than LUMO Rhod band position (−1.42 V vs NHE) which is a good indicative of UV–visible photocatalitic activity efficiency presented by this sample.

In accordance with Fig. 11, N doping of ZnO interfers in the production of impurity and oxygen vacancies in ZnO lattice and, a fundamental difference is the alteration in energetic band levels, not only creating inter band levels between the conduction and valence band, but altering the conduction and Fermi level potential, promoting or enhancing photocatalytic activity under visible illumination. Moreover, ZnO:N conduction band is more negative than hydrogen reduction potential (vs NHE), which is suitable for water splitting apllication.

4. Conclusion

The N doping process affects some properties of ZnO semiconductors, such as photocatalytic activity and crystallite size obtained by XRD measurements. However, the doping process did not affect nanoparticle morphology and band gap. The principal reason for no modification in the nanoparticle band gap is the formation of *p* type clusters in an *n* type semiconductor lattice caused by O substitution by N or interstitial N in the ZnO lattice. The doping process largely affected photocatalytic activity for Rhodamine-B degradation under UV and visible irradiation. There is an optimum N loading in the ZnO doping process for UV illumination (4% N) and for visible illumination (2% N) photocatalytic activity. The modification in the dye degradation mechanism was confirmed for ZnO:N nanoparticle due to the formation of a *p* type cluster, confirmed by electrochemical impedance spectroscopy and Mott Schottky plots. The radicals involved in ZnO dye degradation mechanism under UV illumination are OH^* and O_2H^*. For ZnO:N samples under UV illumination, the degradation mechanism is occur mainly in direct way by holes. Under visible illumination, the radical OH^* is the principal radical for samples, although, holes and O_2H^* radicals participate only using doping samples. These results enhances the essential comprehension of the photocatalytic activity of *n* type semiconductor doping processes and the modification of the dye degradation mechanism.

Acknowledgments

We appreciate the financial support from National Counsel of Technological and Scientific Development (CNPq) (151177/2013) from Brazil, Coordenação de Aperfeiçoamento de Pessoal de Nível Superior (CAPES) from Brazil and Brazilian Agricultural Research

Corporation (EMBRAPA Instrumentation). We also acknowledge Brazilian Nanotechnology Laboratory for Research in Energy and Materials for the technical support during the X-ray photoelectron spectroscopy work.

References

[1] M. Klavarioti, D. Mantzavinos, D. Kassinos, Removal of residual pharmaceutical from aqueous system by advanced oxidation processes, Environ. Int. 35 (2009) 402–417.
[2] R.F.P. Nogueira, W.F. Jardim, Heterogeneous photocatalysis and its environmental applications, Quimica Nova 21 (1998) 69–72.
[3] R. Vinodkumar, I. Navas, K. Porsezian, V. Ganesan, N.V. Unikrishnan, V.P.M. Pillai, Structural spectroscopic and electrical studes of nanostrutured porous ZnO thin film prepared by pulsed laser deposition, Spectrochim. Acta A 118 (2014) 724–732.
[4] T. Prakash, R. Jayaprakash, C. Espro, G. Neri, E.R. Kumar, Effect of Sn doping on microstructural and optical properties of ZnO nanoparticles synthesized by microwave irradiation method, J. Mater. Sci. 49 (2014) 1776–1784.
[5] C. Wu, Y.C. Zhang, Q. Huang, Solvolthermal synthesis of N-doped ZnO microcrystals from commercial ZnO powder with visible light-driven photocatalytic activity, Mater. Lett. 119 (2014) 104–106.
[6] A. Mohanta, J.G. Simmons Jr., H.O. Everitt, G. Shen, S.M. Kim, P. Kung, Effect of pressure and Al doping on strucutural and optical properties of ZnO nanowires synthesized by chemical vapor deposition, J. Lumin. 146 (2014) 470–474.
[7] Y.M. Hao, S.Y. Lou, S.M. Zhou, R.J. Yuan, G.Y. Zhu, N. Li, Structural, optical, and magnetic studies of manganese-doped zinc oxide hierarchical microspheres by self-assembly of nanoparticles, Nanoscale Res. Lett. 7 (2012) 100.
[8] C. Bundesmann, M. Schubert, D. Spemann, T. Butz, M. Lorenz, E.M. Kaidashev, M. Grundmann, N. Asheknov, H. Neumann, G. Wagner, Infrared dieletric functions and phonon modes of wurtzite $Mg_xZn_{1-x}O_{(x \leq 0.2)}$, Appl. Phys. Lett. 81 (2002) 2376–2378.
[9] A. Catellani, A. Ruini, G. Cicero, A. Calzolari, First principles description of the electronic properties of doped ZnO, Phys. Status Solids B 250 (10) (2013) 2106–2109.
[10] N.R. Panda, B.S. Acharya, P. Nayak, Sonochemical synthesis of nitrogen doped ZnO nanorods: effect of anion on growth and optical properties, J. Mater. Sci.: Mater. Lett. 24 (2013) 4043–4049.
[11] V. Vo, T.P.T. Thi, H.Y. Kim, S.J. Kim, Facile post-synthesis and photocatalytic activity of N-doped ZnO-SBA-15, J. Phys. Chem. Solids 75 (2014) 403–409.
[12] C. Li, J. Li, S.S. Li, J.B. Xia, S.H. Wei, Selection rule of preferred doping site for n-type oxides, Appl. Phys. Lett. 100 (2012) 262109, http://dx.doi.org/10.1063/1.4731766.
[13] M. Samadi, M. Zirak, A. Naseri, E. Khorashadizade, A.Z. Moshfegh, Recent progress on doped ZnO nanostructures for visible-light photocatalysis, Thin Solid Films (2016), http://dx.doi.org/10.1016/j.tsf.2015.12.064.
[14] G. Rokicki, A. Piotrowska, A new route to polyurethanes from ethylene carbonate diamines and diols, Polymer 43 (2002) 2927–2935.
[15] S.G. Feng, G.R. Roof, E.Y.X. Chen, Lantalum (V)-based metallocene, half-metallocene, and non-metallocene complexes as ethylene-1-octene copolymerization and methyl methacrylate polymerization catalysts, Organometallics 21 (2002) 832–839.
[16] B.D. Cullity, S.R. Stock, Elements of X-Ray Diffraction, third edition, Prentice Hall, Inc., New Jersey, 2011.
[17] J. Cao, B. Luo, H. Lin, B. Xu, S. Chen, Thermodecomposition synthesis of WO_3/H_2WO_4 heterostructures with enhanced visible light photocatalytic properties, Appl. Catal. B 111–112 (2012) 288–296.
[18] G.B. Soares, B. Bravin, C.M.P. Vaz, C. Ribeiro, Facile synthesis of N-doped TiO_2 nanoparticle by a modified polymeric precursor method and its photocatalytic properties, Appl. Catal. B 106 (2011) 287–294.
[19] M. Dawson, G.B. Soares, C. Ribeiro, Influence of calcination parameters on the synthesis of N-doped TiO_2 by the polymeric precursors method, J. Solid State Chem. 215 (2014) 211–218.
[20] A. Meng, X. Li, X. Wang, Z. Li, Preparation, photocatalytic properties and mechanism of Fe or N-doped Ag/ZnO nanocomposites, Ceram. Int. 40 (2014) 9303–9309.
[21] N.R. Yogamalar, M. Ashok, A.C. Bose, Blue emission and bandgap modification in N:ZnO nanorods, Funct. Mater. Lett. 4 (2011) 271–275.
[22] K. Jindal, M. Tomar, V. Grupta, Inducing electrocatalytic functionality in ZnO thin film by N doping to realize a third generation uric acid biosensor, Biosens. Bioelectron. 55 (2014) 57–65.
[23] T.S. Jeong, J.H. Yu, H.S. Mo, T.S. Kim, C.J. Young, K.J. Hong, Characteristic properties of Raman scattering and photoluminescence on ZnO crystals doped through phosphorous-ion implantation, J. Appl. Phys. 115 (2014) 53521.
[24] J. Lu, Q. Zhang, J. Wang, F. Saito, M. Uchida, Synthesis of N-doped ZnO by grinding and subsequent heating ZnO-urea mixture, Powder Technol. 162 (2006) 33–37.
[25] S. Khosravi-Gandomani, R. Yousefi, F. Jamali-Sheini, N.M. Huag, Optical and electrical properties of p-type Ag-doped ZnO nanostructures, Ceram. Int. 40 (2014) 7957–7963.
[26] B. Liu, X. Zhao, L. Wen, The structural and photoluminescence studies related to the surface of the TiO_2 sol prepared by wet chemical method, Mater. Sci. Eng. B 134 (2006) 27–31.
[27] X. Li, B. Keyes, S. Asher, S.B. Zhang, S.H. Wei, T.J. Coutts, S. Limpijumnong, C.G.V. de Walle, Hydrogen passivation effect in nitrogen-doped ZnO thin films, Appl. Phys. Lett. 86 (2005) 122107–122110.
[28] W.R.L. Lambrecht, A. Boonchun, Identification of a N-related shallow acceptor and electron paramagnetic resonance center in ZnO:N^{2+} on the Zn site, Phys. Rev. B 87 (2013) 195207.
[29] Z. Yu, L. Yin, Y. Xie, G. Liu, X. Ma, H. Cheng, Crystallinity-dependent substitutional nitrogen doping in ZnO and its improved visible light photocatalytic activity, J. Colloid Interface Sci. 400 (2013) 18–23.
[30] S.R. Kadam, V.R. Mate, R.P. Panmand, L.K. Nikam, M.V. Kulkarni, R.S. Sonawane, B.B. Kale, A green process for efficient lignin (biomass) degradation and hydrogen production via water splitting using nanostrucutures C, N, S-doped ZnO under solar light, RSC Adv. 4 (2014) 60626.
[31] M. Nauoar, I. Ka, M. Gaidi, H. Alawadhi, B. Bessais, M.A. El Khakani, Growth, structural and optoeletronic properties tuning of nitrogen-doped ZnO thin films synthesized by means of reactive pulsed laser deposition, Mater. Res. Bull. 57 (2014) 47–51.
[32] W.T. Wu, L. Shi, Q. Zhu, Y. Wang, G. Xu, W. Pang, N-doped ZnO nano-arrays: a facile synthesis route, characterization and photoluminescence, Mater. Lett. 61 (2007) 4752–4755.
[33] Z.W. Wang, Y. Yue, Y. Cao, Preparation and properties of nitrogen doped p-type zinc oxide films by reactive magnetron sputtering, Vacuum 101 (2014) 313–316.
[34] K.M. Lee, E.S. Lee, B. Yoo, D.H. Shin, Synthesis of ZnO-decorated TiO_2 nanotubes for dye-sensitized solar cells, Electrochim. Acta 109 (2013) 181–186.
[35] A. Mhamdi, A. Labidi, B. Souissi, M. Kahlaoui, A. Yumak, K. Boubaker, A. Amlouk, M. Amlouk, Impedance spectroscopy and sensors under ethanol vpors application of sprayed vanadium-doped ZnO compounds, J. Alloys Compd. 639 (2015) 648–658.
[36] B. Saravanakumar, R. Mohan, K. Thiyagarajan, S.J. Kim, Investigation of UV photoresponse property of Al, N co-doped ZnO film, J. Alloys Compd. 580 (2013) 538–543.
[37] C. Wu, Y.C. Zhang, Q. Huang, Solvothermal synthesis of N-doped ZnO microcrystals from commercial ZnO powder with visible light-driven photocatalytic activity, Mater. Lett. 119 (2014) 104–106.
[38] B. Rajbongshi, A. Ramchiary, S. Samdarshi, Influence of N-doping on photocatalytic activity of ZnO nanoparticles under visible light irradiation, Mater. Lett. 134 (2014) 111–114.
[39] G. Biasotto, M.G.A. Ranieri, C.R. Foschni, A.Z. Simões, E. Longo, M.A. Zaghete, Gas sensor applications of zinc oxide thin film grown by polymeric precursor method, Ceram. Int. 40 (2014) 14991–14996.
[40] H. Qin, W. Li, Y. Xia, T. He, Photocatalytic activity of heterostructures based on ZnO and N-doped ZnO, ACS Appl. Mater. Interfaces 3 (2011) 3152–3156.
[41] S. Kumar, A. Baruah, S. Tonda, B. Kumar, V. Shanker, B. Sreedhar, Cost-effective and eco-friendly synthesis of novel and stable N-doped ZnO/g-C_3N_4 core–shell nanoplates with excellent visible-light responsive photocatalysis, Nanoscale 6 (2014) 4830.
[42] W.S. Chang, C.C. Wu, M.S. Jeng, K.W. Cheng, C.M. Huang, T.C. Lee, Ternary Ag-In-S polycrystalline films deposited using chemical bath deposition for photoelectrochemical applications, Mat. Chem. Phys. 120 (2010) 307–312.
[43] M.C. Huang, T. Wang, W.S. Chang, C.C. Wu, J.C. Lin, T.H. Yen, Influence of dipping cycle on structural, optical and photoelectrochemical characteristics of single phase polycrystalline AgInS2 thin film on ITO prepared by aqueous chemical reaction, J. Alloys Compd. 606 (2014) 189–195.
[44] H. Kim, D. Monllor-Satoca, W. Kim, W. Choi, N-doped TiO2 nanotubes coated with a thin TaO_xN_y layer for photoelectrochemical water splitting: dual bulk and surface modification of photoanodes, Energy Environ. Sci. 8 (2015) 247.
[45] N.P. Herring, L.S. Panchakarla, M.S. El-Shall, P-type nitrogen-doped ZnO nanostructures with controlled shape and doping level by facile microwave synthesis, Langmuir 30 (2014) 2230–2240.